Reaction Chemistry & Engineering

ROYAL SOCIETY OF CHEMISTRY

PAPER

View Article Online
View Journal | View Issue

Check for updates

Cite this: *React. Chem. Eng.*, 2024, **9**, 2915

Dual jet-mixing reactor for fully continuous synthesis of core@shell Au@Ag nanocomposites†

Pinaki Ranadive,[a] Faiz Khan,[a] Jessica O. Winter *[ab] and Nicholas Brunelli *[a]

Received 3rd August 2023,
Accepted 9th August 2024

DOI: 10.1039/d3re00417a

rsc.li/reaction-engineering

The wide-scale production of nanomaterials would benefit from scalable synthetic methods. One class of promising nanomaterials consists of a core@shell structure in which one type of material is used for the core and a second material is grown on the surface to produce a shell. Although these materials are commonly realized in batch, core@shell structures have not yet been widely translated to scalable manufacturing processes. In this work, we investigate the continuous flow synthesis of Au@Ag core@shell nanomaterials using sequential jet-mixing reactors (JMRs). Connecting the two JMRs overcomes challenges with particle instability when the processes are separated. Using synthesis conditions typical for batch methods in the JMR resulted in a non-uniform particle size distribution. Through investigating the synthesis conditions of the Au core, the key parameters affecting the synthesis of well-defined nanoparticles are identified as the concentration of the reducing agent and the inclusion of bovine-serum albumin (BSA) to limit particle aggregation. The concentration of the reducing agent is adjusted to achieve a high yield of Au NPs. The adjusted concentration enabled continuous synthesis of Au@Ag core@shell nanoparticles using BSA as the stabilizing ligand in a dual jet mixing reactor system. Overall, this work provides insights on integrating sequential processes for the synthesis of core@shell nanomaterials.

1. Introduction

Laboratory discoveries of high-performance nanomaterials have the potential to advance our capabilities in many applications including pharmaceuticals,[1] electronics,[2] sensors,[3] and catalysis.[4–6] Yet, these lab-scale discoveries are rarely translated to commercial processes because the batch synthesis methods are difficult to scale up while meeting the demands (*e.g.*, material quality) of an industrial scale process. These limitations for nanomaterial synthesis can be overcome using continuous processes that have rapidly advanced in the last decade.[7] Indeed, transferring the batch synthesis of organic and inorganic nanomaterials to flow provides a multitude of advantages, including narrow particle size distribution, high throughput, reproducibility, and high control over particle morphology and composition.[8–12] Flow syntheses also have the advantage of being scalable compared to batch counterparts.[13] Whereas numerous studies have investigated the flow synthesis of single-component metal or metal-oxide nanoparticles,[14,15] multicomponent nanomaterials are of increasing interest because these materials can have increased performance, increased stability, and reduced cost that are beneficial in applications such as catalysis and biosensing.[16–18] Flow synthesis has been investigated as a method to produce multicomponent nanomaterials, including bimetallic and metal-based core@shell nanoparticles.[19–24] However, most of these syntheses are "seeded syntheses" that are adapted as single-step processes in which seeds of one component of the nanomaterial are pre-synthesized in a separate step.[19–22] Separation of steps involved in multicomponent nanomaterial synthesis into multiple processes can hinder the scalability of the overall synthesis and cause issues with process integration[25] and quality control.[26–28] Scalable synthesis of multicomponent nanomaterials would benefit from an integrated platform for fully continuous bottom-up synthesis. Additional research is necessary to integrate a multi-step nanomaterial synthesis into a single, continuous process.

Conventionally, nanoparticle synthesis has been performed in batch or semi-batch processes. Many nanoparticle synthesis reactions are rapid, even at room temperature.[29] In many cases, the nanoparticle synthesis reaction starts before complete mixing of precursors is achieved,[29] resulting in localized regions of high concentration in batch reactors. The non-uniform conditions generate different nucleation and growth kinetics in

[a] *The Ohio State University, William G. Lowrie Department of Chemical and Biomolecular Engineering, 151 W. Woodruff Ave, Columbus, OH 43210, USA. E-mail: winter.63@osu.edu, brunelli.2@osu.edu; Web: https://twitter.com/OSUChemEProfBru*

[b] *The Ohio State University, Department of Biomedical Engineering, Columbus, OH 43210, USA*

† Electronic supplementary information (ESI) available. See DOI: https://doi.org/10.1039/d3re00417a

inorganic nanoparticle synthesis, resulting in a polydisperse nanoparticle size distribution. Achieving precise control of mixing remains a challenge for scaling up batch methods, yielding products with inconsistent nanoparticle size distribution across different trials.[30] A small nanoparticle size with a narrow distribution can be achieved by controlling nucleation and growth kinetics.

Furthermore, synthesizing core@shell nanomaterials adds a new challenge since the heterogeneous nucleation of the shell material on the core should be favored over the homogeneous nucleation of the material intended for the shell to limit formation of a separate population of new particles. As the goal is to create uniform nucleation and growth conditions, it is critical that mixing occurs on a faster timescale than the timescale for nucleation and growth. Confining the reactor volume and length scale has been demonstrated as an effective way to achieve rapid mixing while operating in a continuous mode for higher productivity scales.[31]

Continuous platforms for multicomponent organic nanomaterials have been investigated previously.[32–36] The multi-inlet vortex mixer (MIVM) has been successfully used for the encapsulation of pesticides and drugs in polymeric nanoparticles.[32,33,37] The MIVM is a modification of the millifluidic confined impinging jet mixer[38,39] with four reagent inlets spaced by 90° impinging at a single central point to yield the product, which flows through a perpendicular exit. This geometry provides flexibility in introducing additional channels for reactant flow, but it allows limited investigation of unequal flowrates in opposing jets because of the need to balance the impingement plane at the center. Additionally, control over the residence time between the addition of reagents is restricted as all reagents impinge simultaneously. Microfluidic devices that allow control over the residence time between reagent addition have enabled the fully continuous synthesis of bimetallic nanoparticles.[34] These studies are promising, provided the chip-based mixers can be scaled-up or scaled-out and potential clogging issues are minimized in the microscale channels. Millifluidic mixers have been used to demonstrate the scalable continuous synthesis of active pharmaceutical ingredients and quantum dots.[23,35] The automation and process control associated with these systems makes them attractive, provided that their synthesis space can be expanded to inorganic nanomaterials, including metals and metal oxides. Lastly, many of these synthesis platforms operate in the segmented flow regime in which droplets of an immiscible liquid or gas are interspersed between droplets carrying the reagents.[23,34,35] The narrow particle size distribution associated with segmented flow is desirable if liquid cross-mixing between individual segments because of wall menisci can be minimized.[36,40]

The jet-mixing reactor (JMR) is an ideal candidate for extension to multi-step syntheses because of its modular design, as has been demonstrated for the gas-phase synthesis of nanomaterials.[41] Specifically, two reactors can be connected in series to provide jet inlets for reagents downstream of the first reactor. The residence time between the two reactors can be controlled through the length of tubing connecting the reactors or by changing the total flowrate. This design is flexible and can enable the synthesis of a range of nanomaterials.

In this work, a dual jet-mixing reactor system is assembled, consisting of two JMRs in series for the synthesis of Au@Ag core@shell nanomaterials as a model system. Au@Ag nanoparticles have been applied in biosensing because of the synergistic plasmon resonance of the Ag shell and the Au NPs.[21] Au@Ag NPs are an ideal system for initial demonstration of multi-step inorganic nanomanufacturing processes as their synthesis takes place at ambient conditions and characterization through UV-vis spectroscopy can provide information about particle size and synthesis yield.[42] Microfluidic and milli-fluidic devices have been investigated for Au@Ag NP synthesis, but these have used a seeded synthesis approach in which Au NPs were pre-synthesized in batch and used as a reagent in a single-step reactor, and thus were not manufactured in a fully continuous process.[21,22,43] We present a fully continuous jet-mixing process for Au@Ag nanoparticle synthesis and compare the properties of jet-mixing synthesized Au@Ag nanoparticles to the lab-scale batch method. Au NP cores are synthesized in a first reactor and are used as seeds for Au@Ag NP synthesis in a separate JMR to form an Au@Ag core@shell nanomaterial. Each step of the process (*e.g.*, core synthesis) is investigated to determine reactant concentrations and conditions that produce high quality nanomaterials. The materials synthesized in batch and *via* jet-mixing are characterized using a combination of dynamic light scattering (DLS), UV-vis absorption, and transmission electron microscopy (TEM) to identify conditions that produce narrow particle size distributions and high yields. These insights are used to design a fully continuous process to synthesize Au@Ag NPs in flow using the dual JMRs. Overall, this work demonstrates fully continuous core@shell NP synthesis and expands the scope of nanoprecipitation manufacturing to multi-step, liquid-phase processes.

2. Experimental methods

2.1. Chemicals

The chemicals are used as received without further purification, including hydrogen tetrachloroaurate(III) trihydrate ($HAuCl_4$; 99.99% metal basis, ACS grade, Fisher Scientific); sodium borohydride powder ($NaBH_4$; 98%, Alfa Aesar); L-ascorbic acid (AA; Macron Fine Chemicals); and silver nitrate ($AgNO_3$; VWR Life Sciences). All solutions are prepared using purified deionized (DI) water. The DI water is filtered by passing once through a nylon syringe filter (0.22 μm, Perkin Elmer) before use.

2.2. Reactor design

2.2.1. Single jet-mixing reactor. The geometry of a single JMR has been adapted from prior work with gas-phase nanomaterial synthesis.[41] We have also used this reactor design successfully for the liquid-phase synthesis of single component ZIF-8 (ref. 29) and Ag NPs,[44] as well as the titania shell of a Pd@TiO_2 composite catalyst.[6] The reactor is constructed in-house from thermally and chemically stable polyether ether ketone (PEEK) in the form of a cube (1″ × 1″ × 1″) with cylindrical channels drilled through for reagent flow, as shown in Fig. 1. The first channel is drilled through the center of the cube and is called the main line (d_{main} = 0.04″ = ~1000 μm). The second channel is drilled such that it perpendicularly intersects the first channel in the center of the cube and comprises the jet lines (d_{jet} = 0.02″ = ~500 μm). The jet lines are constructed such that two opposite-facing jets perpendicularly impinge on the main line. The reactor is constructed by drilling both jets consisting of the jet lines from the same side of the cube to ensure alignment. The channels are threaded at the ends for connecting clear polytetrafluoroethylene (PTFE, ID 0.03″) tubing using PEEK fittings of appropriate size. Two syringe pumps (KD Scientific, 100KD) are used to pump reagents through the main and jet lines: one for the mainline and one for the jet-lines. The line from the syringe pump for the jets is split into two lines through a Y-assembly PEEK fitting, each of which connects to one of the jets. The product solution that consists of the combined jet line and main line streams flows out downstream of the reactor colinear to the main line.

2.2.2. Dual jet-mixing reactor. The dual JMR assembly integrates two identical single jet-mixers (d_{main} = 0.04″; d_{jet} = 0.02″) in series. A diagram of the dual jet-mixing set-up used specifically in this work can be found in Fig. 2 and is further discussed below. PTFE tubing (ID 0.03″) is used throughout the assembly and PEEK microfluidic fittings are used for fluidic connections. The first jet-mixing reactor has main and jet lines identical to the single jet-mixing reactor to introduce two reagents into the system. The outlet from the first reactor has a tubing length of 3 m and is connected to one inlet of a Y-joint fitting. The other inlet of the Y-joint introduces into the reaction mixture the reductant ascorbic acid (AA) (third reagent) to allow mixing of the Au NPs and AA before silver ion reduction. The outlet of the Y-joint is connected to tubing with a length of 1 m and functions as the main line of the second jet-mixing reactor downstream of the first reactor. A pair of jets connected to the second reactor introduces a fourth reagent in the system. The outlet solution from the second jet-mixing reactor is collected as the product. Four separate syringe pumps (KD Scientific, 100KD) are used to deliver the different reagents through the main and jet lines of the two jet-mixers or through the Y-joint. Whereas the flow rate of each reagent can be independently controlled, we only investigate the symmetric flow configurations where the flow rate through jet lines and main line are matched.

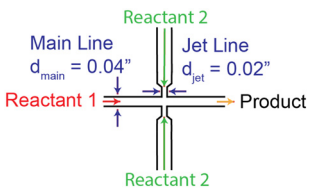

Fig. 1 Geometry of a jet-mixing reactor (JMR) unit with a main line (d_{main} = 0.04″; 1000 μm) carrying reactant 1 and an orthogonally impinging jet line (d_{jet} = 0.02″; 500 μm) consisting of a pair of jets carrying reactant 2. The product is collected downstream of the reactor.

2.3. Batch synthesis of Au NP cores

The procedure for batch synthesis of gold nanoparticles (Au NPs) is based on a room-temperature synthesis in the literature.[45] All solutions are prepared fresh before each synthesis and by weighing all chemicals. An aqueous solution of 0.27 mM $HAuCl_4$ is prepared in filtered DI water. An equal volume of $NaBH_4$ aqueous solution at the desired concentration is prepared in filtered DI water. In a standard synthesis, the $HAuCl_4$ solution (16.5 mL) is added to a 100 mL round-bottom flask with a 1″ PTFE-coated stir-bar stirring at 500 RPM. An equal volume of the $NaBH_4$ solution (16.5 mL) is injected rapidly into the round bottom flask. The stirring is continued for 10 minutes before analysis. No stabilizing ligands are employed in the standard process, which produces seeds for Ag shell growth.

2.4. Batch synthesis of Au@Ag NPs using Au NP seeds

The procedure for the Au NP seeded synthesis of Au@Ag NPs is based on a room-temperature reduction of $AgNO_3$ with ascorbic acid (AA).[20] All solutions are prepared fresh before each synthesis. Au NP cores are synthesized according to the batch procedure above and characterized by UV-vis to confirm that their plasmonic properties are similar to previous syntheses prior to use. The Au NPs are aged by 10 minutes before use. Separately, a stock solution is prepared of AA (0.035 g) in filtered DI water (10 g). A reagent solution of the desired AA concentration is prepared by diluting the stock with the required weight of filtered DI water. Another stock solution is prepared of $AgNO_3$ (0.015 g) in filtered DI water (20 g). A reagent solution of 0.062 mM $AgNO_3$ is prepared by mixing the stock (0.106 g) with filtered DI water (7.394 g). In a standard batch, Au NP cores (0.5 mL) are mixed with AA solution (4.5 mL) prior to synthesis and added to a 25 mL round-bottom flask with a 1/2″ PTFE-coated stir-bar stirring at 200 RPM at room temperature. $AgNO_3$ solution (5 mL) is rapidly added to the Au NP cores – AA solution within 10 seconds. The product solution is aged for 5 minutes with continuous stirring prior to analysis.

2.5. Jet-mixing synthesis of Au NPs

The jet-mixing synthesis of Au NP cores is performed using a 0.27 mM $HAuCl_4$ aqueous solution and $NaBH_4$ aqueous solution of desired concentration. Equal volumes of the solutions are filled in separate 60 mL HSW Luer-Lok syringes.

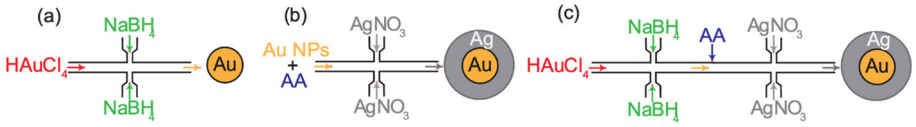

Fig. 2 Assembly of the jet-mixing system for: (a) Au NP core synthesis using a single jet-mixing reactor; (b) seeded Au@Ag NP synthesis using a single jet-mixing reactor and Au NP seeds pre-synthesized in batch; and (c) fully continuous Au@Ag NP synthesis using two single jet-mixing reactors in series with a Y-joint between the reactors to introduce ascorbic acid (AA). The geometry of the jet-mixing reactor for all set-ups is similar consisting of a main line (d_{main} = 0.04 inch) carrying one reactant and jet lines (d_{jet} = 0.02 inch) carrying a second reactant. Each reagent is delivered through a separate syringe pump. All syntheses are performed using the following reagent concentrations: 0.27 mM $HAuCl_4$, 0.9 mM $NaBH_4$, 0.062 mM $AgNO_3$, and 8 mM AA. For seeded Au@Ag NP synthesis, Au NPs (10% by volume) are dissolved in AA prior to starting the jet-mixing run.

The syringe containing the $HAuCl_4$ solution is connected to the main line of the single jet-mixing reactor, and the syringe containing the $NaBH_4$ solution is connected to the jet lines. The flowrate of each syringe pump is set to the desired value such that the flow rates in the main line and jet lines are equal. The first few drops (1–2 mL) of product solution are discarded to avoid collecting particles resulting from unsteady state flow. The product is collected downstream in a beaker before analysis. The single jet-mixing setup for Au NP core synthesis is shown in Fig. 2a.

2.6. Single-jet mixing synthesis of Au@Ag NPs using Au seeds

The reagent solutions for the jet-mixing synthesis of seeded Au@Ag NPs are prepared in a similar manner to the batch synthesis. Initially, a single jet-mixing reactor is used for seeded synthesis to optimize shell growth independently. The $AgNO_3$ reagent solution (0.062 mM) is filled into a 5 mL (HSW Luer-Lok) syringe that is connected to the jet lines of the jet-mixing reactor. An equal total volume of the reagent solution containing AA of the desired concentration (4.5 mL) pre-mixed with Au NPs (0.5 mL) synthesized in batch is filled into a separate syringe that is connected to the main line. The flowrate of each syringe pump is set to 48 mL h^{-1}. The product is collected downstream after discarding the initial output (2–3 mL) from unsteady state operation and analyzed after collection. The single jet-mixing set up for Au@Ag NP synthesis is shown in Fig. 2b.

2.7. Fully continuous dual jet-mixing synthesis of Au@Ag NPs

Reagent solutions of $HAuCl_4$, $NaBH_4$, AA, and $AgNO_3$ are prepared in a manner similar to the one-pot batch synthesis with comparable reagent concentrations to the batch. All solutions are filled into separate syringes (HSW Luer-Lok, 20 mL). The set-up of the dual jet-mixing synthesis of Au@Ag NPs is shown in Fig. 2c. The $HAuCl_4$ solution and $NaBH_4$ solutions are connected to the main and jet lines, respectively, of the first jet-mixing reactor in the dual jet-mixing assembly with a flowrate of 48 mL h^{-1} set for each of the lines. The outlet from the first reactor is connected to the inlet of a Y-joint. The AA solution is connected to the second inlet of the Y-joint between the two jet-mixing reactors with a flowrate of 96 mL h^{-1}. The outlet from the Y-joint is connected to the main line of the second downstream reactor. The $AgNO_3$ solution is connected to the jet lines of the second reactor and its flowrate is set to 192 mL h^{-1}. The ratio of the flowrates of the reagents is set such that their concentrations after mixing in the reactor are comparable to those obtained in the one-pot batch synthesis. Initially, only the reagents entering the first reactor are pumped and sufficient time is allowed for the Au NPs to reach steady state (~10 min). During this stage, the outlet of the first reactor is disconnected from the inlet of the second. Next, the reactors are connected and the flow for AA and $AgNO_3$ is started. The product is collected at the outlet after allowing the system to reach steady state (1–2 min).

2.8. Material characterization

The materials are characterized using a combination of UV-vis spectroscopy (UV-vis), dynamic light scattering (DLS), and transmission electron microscopy (TEM). The Au NP cores are characterized using UV-vis within 10 minutes of synthesis for their plasmonic properties and DLS within an hour of synthesis for particle size. The Au@Ag NP samples are characterized using UV-vis. Batch-synthesized samples are characterized after 5 minutes of synthesis, and jet-mixing-synthesized samples are characterized immediately after synthesis such that the aging time in both processes is comparable.

UV-vis analysis is performed using a ThermoFisher Evolution 300 UV-vis spectrophotometer with a Xenon lamp using a bandwidth of 2 nm, scan speed of 600 nm min^{-1} in a 1 cm pathlength quartz cuvette. DI water is used as a reference baseline. Peaks in the UV-vis spectra of Au@Ag NPs are deconvoluted using the multi-peak fitting function in IGOR Pro 8. The particle size distribution (PSD) for Au NPs is determined through DLS using a Brookhaven Instruments Corporation BI-200SM Goniometer and a 637 nm laser beam at a detector angle of 90° with a dust cut-off of 20 μm. The solvent is set as water, and the temperature is set to 20 °C. Three runs are conducted for each sample with the average being recorded to calculate the PSD. Analysis is performed *via* the Brookhaven Instruments Dynamic Light Scattering software.

Transmission electron microscopy (TEM) is used to visualize the NP shape and to quantify the particle size distribution. In the absence of stabilizing ligands, it is observed that NPs form agglomerates. Hence, the Au NP cores are stabilized through collecting an equal volume of NP

solution exiting the JMR with an equal volume of bovine serum albumin (BSA) (1 mg mL^{-1}; cooled to 4 °C). TEM imaging is performed using a FEI Tecnai G2 Spirit TEM at a voltage of 80 kV in bright-field mode. TEM samples are prepared on 150 mesh holey-carbon copper grids. The grids are plasma discharged using a PELCO easiGlow™ glow discharge cleaning system through one cycle. The NP solution (10 μL) is dropped on the cleaned grid and air-dried in a partially covered petri dish for 4 hours prior to analysis. The images are analyzed using ImageJ[46] to determine the particle size and size distribution.[47] The TEM particle size distribution data are fit to a lognormal distribution and parameters such as mean Feret length and standard deviation for NP are determined according to methods described in literature.[48] Details for yield calculation of Au NPs are given in the ESI† in section S4. The structural composition of Au@Ag NPs is analyzed using ThermoFisher Scientific/FEI Tecnai F20 at 200 kV with an EDAX XLT windowless SDD EDX detector.

3. Results and discussion

3.1. Direct translation of Au@Ag batch concentration conditions to jet-mixing synthesis

Au@Ag NPs are synthesized using comparable reagent concentrations in both a batch and a continuous jet-mixing process. As a basis, a two-step batch synthesis method is used to produce Au@Ag NPs. The core Au NPs are synthesized in batch using a $NaBH_4$ (2.4 mM) reduction-based, stabilizing ligand-free synthesis from the literature.[45] The UV-vis spectrum obtained for the Au NPs along with a representative TEM image are shown in Fig. S1.† The plasmonic peak at 515 nm confirms the presence of Au NPs, and DLS particle size analysis results in a size distribution of 9 ± 1 nm consistent with prior reports.[49]

The Au NPs are used as seeds for Au@Ag NP synthesis *via* ascorbic acid (AA) reduction of $AgNO_3$.[20] Batch synthesis is performed using reagent concentrations of 0.062 mM $AgNO_3$, 2 mM AA, and 5% Au by volume in the final solution. Comparable final concentrations are used for the JMR synthesis of Au@Ag NPs. A representative TEM image associated with the batch syntheses is shown in Fig. 3a. There is an increase in particle size compared to the Au NPs used as seeds (Fig. S1†), suggesting the formation of a core@shell morphology. In addition, numerous small particles and large aggregates are also observed. For the batch synthesized sample, it is possible to measure the size of individual particles to obtain a particle size distribution, but the particles are agglomerated. The agglomeration indicates the particles produced using the batch process are polydisperse. Regardless of polydispersity, it is possible to observe particles with contrast differences between the core and the shell regions, as highlighted by circles in Fig. 3a. The contrast difference is consistent with the expected Z-atomic number difference between Ag and Au materials that is suggestive of multicomponent core@shell material.[50]

To compare to the batch method, a single JMR is used to form Au@Ag NPs. The seeded, jet-mixing-synthesized Au@Ag NPs include similar large particles with the increased presence of secondary smaller particles, as shown in Fig. 3b. Qualitatively, the TEM image contains both small (~10 nm) and large (~50 nm) particles. The results for batch and JMR synthesis are comparable with both synthesis methods producing large core@shell particles and small particles, but it appears that the JMR produces more smaller particles compared to the batch process. The polydispersity is problematic and could be associated with agglomeration. Hence, further work focuses on studying the synthesis parameters in each step of the batch synthesis of Au@Ag NPs with the goal of adapting it to a continuous process and minimizing the formation of a secondary particle population.

3.2. JMR synthesis of Au NPs

The synthesis of Au NPs is investigated to determine the range of conditions for which uniform NP cores are formed.

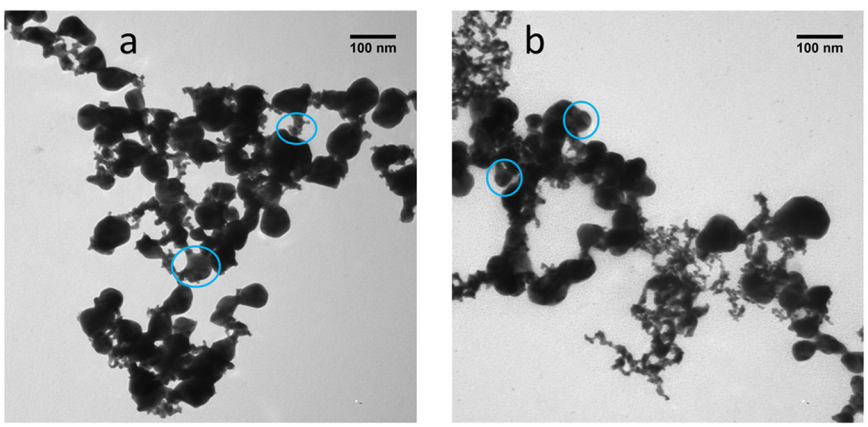

Fig. 3 TEM images of: a. batch; b. jet-mixing, seeded Au@Ag NPs synthesized using 0.062 mM $AgNO_3$, 2 mM ascorbic acid, and 5% by volume Au NPs in the product solution.[20] Au NPs are synthesized in batch with 0.27 mM $HAuCl_4$ and 2.40 mM $NaBH_4$, as given in literature.[45] The single jet-mixing reactor synthesis is performed at main line and jet line flowrates of 48 mL h^{-1}.[29,30] The blue circles correspond to areas of Z-contrast.

Au NPs are synthesized through aqueous phase reduction of $HAuCl_4$ by $NaBH_4$ in the absence of a stabilizing ligand. The goal is to identify the concentration of $NaBH_4$ that produces a high yield of Au NPs. Multi-step flow processes typically benefit from high-yield upstream operations that require minimal downstream purification, as installation of in-line separation or purification devices remains challenging.[51] It is hence important to develop a high-yield Au NP synthesis procedure with maximum consumption of $HAuCl_4$ before the downstream shell formation with Ag occurs in the dual jet-mixer. Typical single component aqueous-phase NP syntheses involve excess $NaBH_4$ compared to the nanoparticle precursor to promote nucleation.[45,52,53] Excess $NaBH_4$ remaining in the dual jet-mixer after Au NP synthesis may influence downstream capping of Ag around the Au cores. Specifically, $NaBH_4$ is a stronger reducing agent compared to AA that is introduced downstream to promote the heterogeneous nucleation of Ag around the Au NP seeds.[54] Excess $NaBH_4$ may result in fast reduction of $AgNO_3$ and promote homogeneous Ag NP nucleation in addition to heterogeneous nucleation on Au NP cores. Hence, it is desirable to minimize the $NaBH_4$ concentration remaining downstream after Au NP synthesis. Refining the procedure for Au NP synthesis focuses on achieving high Au NP yield at minimal use of $NaBH_4$. The results for batch synthesis of Au NPs with different $NaBH_4$ concentrations are presented in the ESI† (section S2).

Following this optimization step, Au NPs are synthesized *via* single jet-mixing with 0.9 mM $NaBH_4$ and other reagent concentrations comparable to the batch synthesis using main line and jet lines flowrates of 48 mL h^{-1}. The UV-vis spectrum of the Au NPs obtained *via* jet-mixing is shown in Fig. S2† along with that of the batch-synthesized Au NPs for comparison. Jet-mixing synthesized Au NPs have a maximum absorbance wavelength around 530 nm, a longer wavelength than that obtained for the batch-synthesized counterpart, suggesting larger Au NPs or increased aggregation in the jet-mixing reactor *vs.* batch synthesis.[55] The absorbance value associated with the jet-mixing synthesized sample is also lower than that obtained for the batch-synthesized sample. The decrease in absorbance may be associated with either a change in particle concentration or extinction coefficient because of a change in particle size.

The Au NPs synthesized by jet-mixing are further analyzed by DLS and TEM to compare the particle size with the batch-synthesized Au NPs. A representative TEM image of Au NPs synthesized through jet-mixing is shown in Fig. 4. Size analysis is not performed on these samples as Au NPs formed in the absence of stabilizing ligands are susceptible to agglomeration after synthesis. Hence, DLS as well as TEM might not capture an accurate representation of the particle size distribution. Accordingly, the synthesis method is modified to add a stabilizing ligand in the collection flask to enable these analyses.

To address agglomeration, the Au NPs from the JMR are collected into BSA aqueous solution cooled to 4 °C. The low temperature is expected to minimize further reduction. BSA has been shown to cap the particles, enabling capture of a frozen snapshot of the NP size as it exits the JMR.[56] A $NaBH_4$ concentration optimization study is conducted in the JMR, similar to the batch experiments. The UV-vis spectra of BSA-stabilized Au NPs synthesized using $NaBH_4$ concentrations ranging from 0.6 to 2.4 mM are depicted in Fig. 5. The Au NPs have peaks around 520–525 nm, suggesting that the NP size is minimally affected by the $NaBH_4$ concentration. The absorbance peak value increases with increasing $NaBH_4$ concentration, indicating increased reduction of Au^{3+} to Au^0.

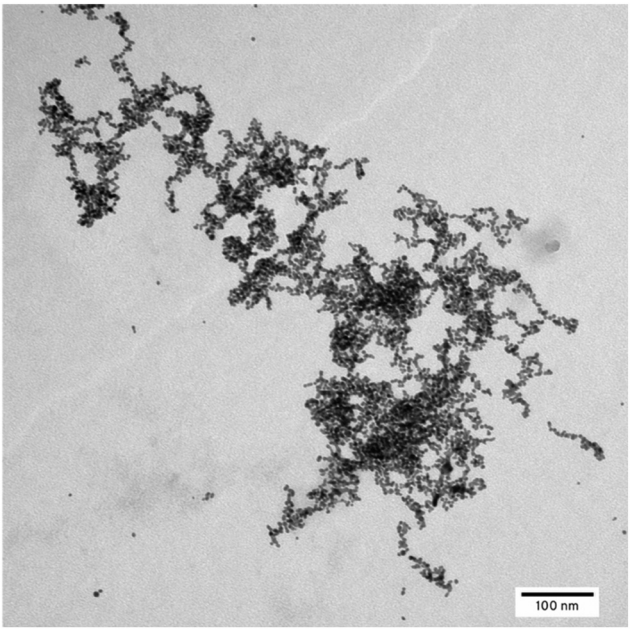

Fig. 4 TEM images of Au NPs synthesized in jet-mixing with 0.90 mM $NaBH_4$ and 0.27 mM $HAuCl_4$ in absence of stabilizing ligand. The main line and jet line flowrates in the single jet-mixer are maintained at 48 mL h^{-1}.

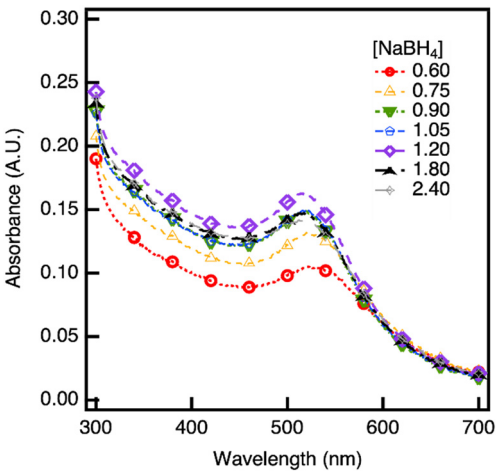

Fig. 5 UV-vis spectra of Au NPs synthesized *via* jet mixing reactor with different concentrations of $NaBH_4$ and 0.27 mM $HAuCl_4$ with the addition of BSA post-synthesis.

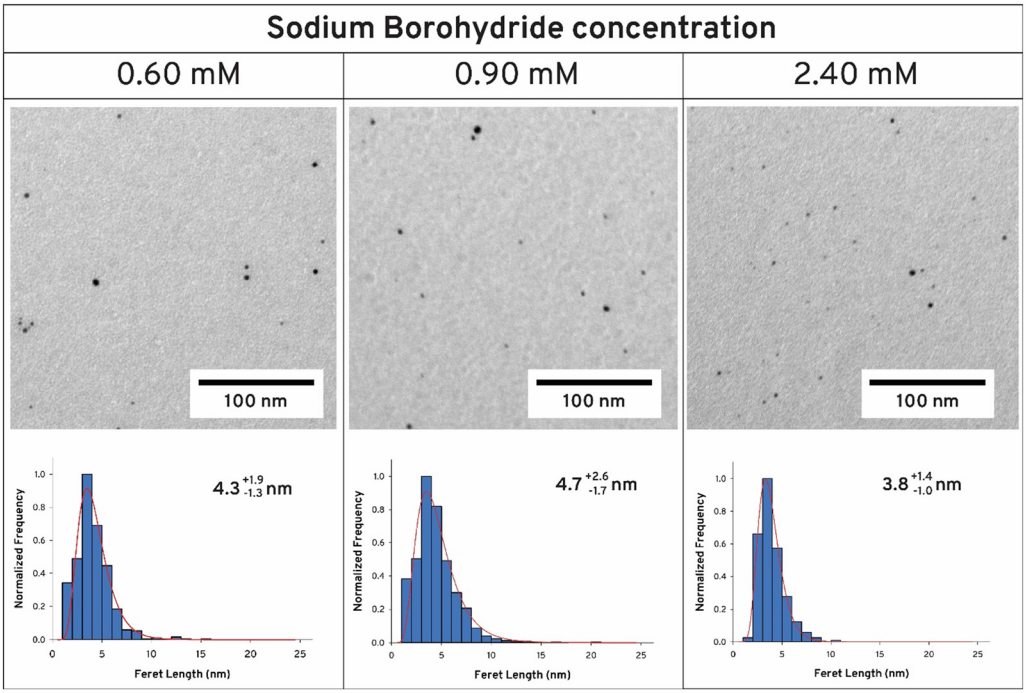

Fig. 6 TEM images of Au NPs synthesized *via* jet mixing reactor at 0.27 mM $HAuCl_4$ and different concentrations of $NaBH_4$ with post-synthesis addition of a cold BSA aqueous solution.

The particle size is analyzed from TEM images with representative images shown in Fig. 6. BSA prevents Au NP agglomeration and enables counting of 500+ individual, non-aggregated particles at each reaction condition to determine a particle size distribution. A summary of the TEM particle size distribution and yield calculations (determined as ESI† S4) are provided in Table 1. From TEM, it is observed that increasing $NaBH_4$ concentration does not significantly affect mean Au NP size, which remains in the range of 3.7–4.8 nm. This smaller size (*versus* that observed in Fig. S2 and S3†) reflects the stabilization provided by the BSA capping ligand. The absorbance peak data further supports this conclusion, as the peaks are consistently between 520–525 nm (Fig. 5).

As the $NaBH_4$ concentration is increased from 0.6 to 0.9 mM, the yield increases from 64% to 90%. Further increase in reducing agent concentration does not noticeably increase the yield, as the UV-vis data are consistent with the majority of Au^{3+} reduction (~90%) being complete with 0.9 mM $NaBH_4$ solution.

Table 1 Effect of $NaBH_4$ concentration on Au NP size and yield as synthesized in the JMR. The $HAuCl_4$ concentration is maintained constant in all syntheses at 0.27 mM. The sample is collected into a flask with cold BSA as the stabilizing ligand. The particle size distribution was captured by counting 500+ particles in TEM images

[$NaBH_4$] (mM)	Mean Feret length (nm)	Positive Std.	Negative Std.	Yield (%)
0.60	4.3	1.9	1.3	64
0.75	4.8	2.0	1.4	78
0.90	4.7	2.6	1.7	90
1.05	4.8	2.0	1.4	90
1.20	4.0	1.6	1.1	104
1.80	3.7	1.5	1.1	98
2.40	3.8	1.4	1.0	93

3.3. Au@Ag NP fully continuous synthesis

The seeded synthesis of Au@Ag NPs is investigated for both batch and jet-mixing conditions to optimize the concentration of the reducing agent ascorbic acid. These results are presented in the ESI† (section S5). These seeded synthesis results are used to inform the synthesis of the fully continuous process, whereby Au@Ag NPs are synthesized in a single process involving two jet-mixing reactors placed in series, as shown in Fig. 2c.

The dual jet-mixing reactor assembly consists of a primary single jet-mixer for Au NP synthesis with a second jet-mixer in series for subsequent capping of the Au NPs with the Ag shell. AA is introduced between the two jet-mixers for heterogeneous $AgNO_3$ reduction. Different particle morphologies could be expected if both AA and $NaBH_4$ are used for reduction simultaneously. Silver nanoprisms have been synthesized by using sodium borohydride to reduce silver nitrate or by adding a range of concentrations of AA from 0–50 mM to control growth to triangular structures.[57] Gold nanourchins have been synthesized through controlling the molar ratio of $NaBH_4$: AA : $HAuCl_4$ to 1 : 1 : 1 at an acidic pH = 2. Synthesis of spherical NPs typically requires the presence of only one of the reducing agents.[58] Hence, the reducing agents have not been added simultaneously with $HAuCl_4$ to promote the growth of spherical Au NPs in the

dual jet-mixing reactor. Additionally, adding AA and $AgNO_3$ downstream of the $NaBH_4$ and $HAuCl_4$ allows for growth of the Au NPs before capping with Ag.

The design for dual jet-mixing assembly is such that the concentrations after mixing of $AgNO_3$, AA, and Au NPs are comparable to those used in the seeded jet-mixing and batch syntheses so that insights gained on Ag capping can be translated to the fully continuous synthesis. It is desirable to maintain the same flowrates in each line of the downstream jet-mixing reactor in which Ag capping is achieved. It is also preferable to maintain equal flowrates in the main line and jet line of the upstream jet-mixer, as previous work with equal jet-mixing flowrates has shown an improvement in NP properties, including the particle size distribution and stability.[29,30] The dual jet-mixing system is hence modified to incorporate a flowrate of 48 mL h^{-1} in the lines of the upstream JMR, as these main line and jet lines flowrates have resulted in successful Au NP synthesis, as demonstrated in section 3.2. This results in an output flowrate of 96 mL h^{-1} Au NPs from the upstream jet-mixer. To maintain equal main line and jet lines flow rates in both reactors, the flow rates are maintained at 96 mL h^{-1} for AA and 192 mL h^{-1} for $AgNO_3$. The initial concentration of AA is adjusted such that the concentration after mixing downstream of the second reactor is comparable to that for the seeded synthesis (ESI† section S5). However, the concentration of Au NPs after mixing changes from 5% by volume in the product to 25% by volume with this modification. This synthesis is regarded as a proof-of-concept demonstration to which further changes in parameters can be made for optimization of Au@Ag NP properties. The selected reagent concentrations before and after mixing in the dual jet-mixing assembly are shown in Table 2. Essentially, the dual jet mixing apparatus represents a sequential nanoprecipitation process conducted using two JMRs in series operation.

In the absence of stabilizing agent, Au@Ag NPs prepared using dual JMRs exhibit aggregated nanostructures (Fig. S12a†), and the particle size distribution is difficult to quantify. Energy dispersive X-ray (EDX) mapping analysis (Fig. S12b–e†) indicate the presence of both Au and Ag. Based on relative EDX peak intensities, there is a higher presence of Ag relative to Au. (The observed copper peaks result from copper-based TEM grids. Such issues commonly arise when working with copper grids and could be eliminated with the use of beryllium grids.[57]) The presence of aggregated structures limits quantification of shell thickness. Hence, a similar experiment with dual JMRs was repeated with addition of cold BSA to the outlet core–shell NPs to stabilize the product.

TEM analysis (Fig. 7) of 250+ individual particles is performed to determine a particle size distribution. Whereas some non-spherical elongated particles are observed, images show the formation of mostly core@shell spherical NPs. The core@shell structure can be observed because of the Z-contrast differences between Au and Ag, causing the Au cores to appear darker than the Au shells with example core@shell structures observable in Fig. 7b. The mean Feret length for Au@Ag NPs is 10.1 nm, an increase from 4.7 nm for Au NPs stabilized with BSA (Table 1). The elongated nanostructures constitute a secondary peak (~22 nm) in the particle size distribution obtained through TEM. As most of the NPs appear spherical, the size increase suggests an average Ag shell thickness ~2.7 nm. The particle size distribution has a polydispersity of 0.33, which can be decreased with the *in situ* inclusion of appropriate stabilizing ligands. However, this could also modify the nucleation and growth dynamics of the reaction.

The increase in NP size (Fig. 7) and the EDX analysis (Fig. S12†) are consistent with the formation of Au@Ag core@shell nanocomposites using dual JMRs. This synthesis is a proof-of-concept demonstration for sequential JMR flow synthesis of core@shell nanoparticles.

3.4. Controlling Au@Ag NP properties through dual jet-mixing

Operational parameters including input flow velocities, precursor and ligand concentration, and the jet-mixing reactor configuration can be further optimized to achieve the desired Au@Ag NP size properties. Controlling the concentrations of Au^{+3}, Ag^{+}, AA, and $NaBH_4$ at points of mixing in the reactor leads to control over the relative rates of homogeneous and heterogeneous nucleation. Balancing these rates is key to controlling the composition, purity, and particle size distribution of Au@Ag NPs. Specifically, the rates of three processes need to be considered: (1) homogeneous

Table 2 Reagent concentrations before mixing and after mixing for the modified dual Au@Ag NP JMR synthesis, according to selected process parameters. All reagent concentrations after mixing for the dual JMR system are reported downstream of the second jet-mixing reactor. The concentrations used for starting reagents are: 0.27 mM $HAuCl_4$, 0.90 mM $NaBH_4$, 16 mM ascorbic acid (AA), and 0.062 mM $AgNO_3$

Process	Reagent	Initial concentration (mM) (C_i)	Flowrate (mL h^{-1}) (Q_i)	Concentration after mixing (mM) $\left(\frac{C_i Q_i}{\sum Q_i}\right)$
Modified dual JMR[a]	$HAuCl_4$	0.27	48	1.43×10^{-6} Au NPs
	$NaBH_4$	0.90	48	
	AA	15	96	3.6
	$AgNO_3$	0.062	192	0.031

[a] Starting solutions of $HAuCl_4$ (0.27 mM) and $NaBH_4$ (0.90 mM) at a jet-mixing flowrate of 48 mL h^{-1} each result in Au NP concentrations of 5.7×10^{-6} mM exiting the upstream jet-mixer at 96 mL h^{-1}. These values are used for subsequent concentration calculation after mixing.

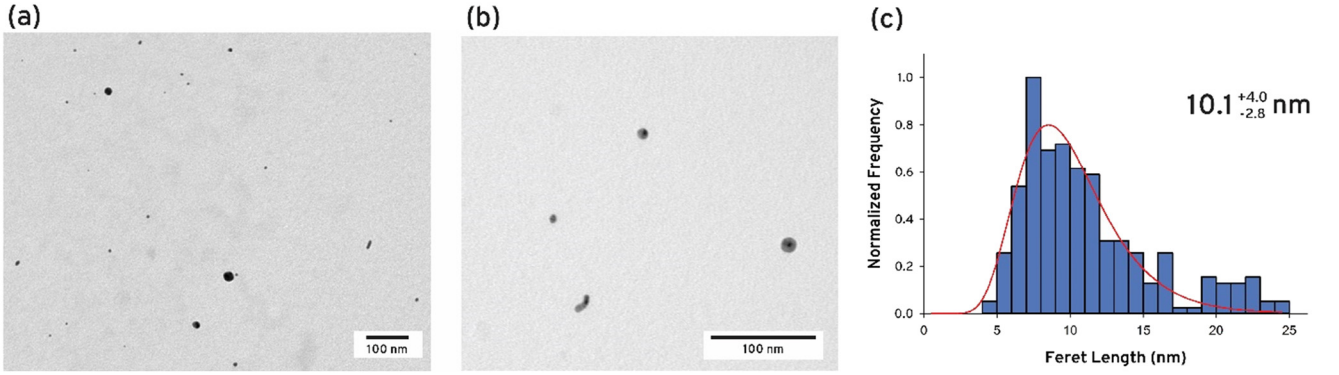

Fig. 7 (a) and (b) Representative TEM images of Au@Ag NPs synthesized *via* dual JMRs in series operation and (c) particle size distribution with lognormal fitting (number of particles counted: 250+). The particles are synthesized using the experimental conditions in Table 2, including 0.27 mM $HAuCl_4$, 0.90 mM $NaBH_4$, 15 mM AA, and 0.062 mM $AgNO_3$ with flow rates of 48 mL h^{-1} into the first JMR of $HAuCl_4$ (jet) and $NaBH_4$ (main) followed by mixing the combined stream with 96 mL h^{-1} of AA (y-mixer) and 192 mL h^{-1} of $AgNO_3$ (jets).

Au NP formation; (2) homogeneous Ag NP formation; (3) heterogeneous Ag shell formation. The JMR can be designed and operated to enable production of the desired structure. For example, the main and jet line diameters of the dual jet-mixing reactor can be selected to enable the desired productivity while maintaining the necessary mixing intensity. Overall, the flexibility of operation makes the jet-mixing reactor promising for the synthesis of controlled core–shell or multicomponent nanoparticles because of its flexible and adaptable design that can be tailored for the synthesis of particles with specific desired properties. Additionally, it would be possible to decrease the polydispersity through operating the system with asymmetric flow filtration to purify the product stream.[58,59]

4. Summary

The synthesis of core@shell Au@Ag nanoparticles is demonstrated using a fully continuous process with jet-mixing reactors in series. The first JMR is used to produce the Au NPs cores. In the absence of a stabilizing ligand, the results for the JMR and batch processes are similar showing a number of large particles with aggregation. Using BSA as a stabilizing ligand in the collection flask, the JMR produces Au cores with an average size ~4 nm. Through varying the synthesis conditions, it is found that the JMR can produce a high yield of Au NPs with minimum residual reducing agent at a sodium borohydride concentration of 0.9 mM. Further optimization was performed using Au NP seeds to identify the optimal concentration of ascorbic acid for $AgNO_3$ reduction as 8 mM. These conditions are implemented in a fully continuous JMR synthesis, resulting in the formation of Au@Ag nanoparticles confirmed *via* size increases observed in TEM and changes in composition observed in EDX elemental analysis. This study provides a roadmap for optimization of future core@shell nanomaterials synthesis using integrated flow reactors. This work demonstrates that the scope of jet-mixing can be expanded to include multi-step nanomaterial syntheses, toward continuous manufacturing paradigms.

Conflicts of interest

There are no conflicts to declare.

Acknowledgements

The authors acknowledge support from the National Science Foundation (CMMI 211412).

References

1 A. Aghebati-Maleki, S. Dolati, M. Ahmadi, A. Baghbanzhadeh, M. Asadi, A. Fotouhi, M. Yousefi and L. Aghebati-Maleki, *J. Cell. Physiol.*, 2020, **235**, 1962–1972.
2 D. M. Holunga, N. A. Brunelli and R. C. Flagan, *J. Nanopart. Res.*, 2013, **15**, 2027.
3 M. Segev-Bar and H. Haick, *ACS Nano*, 2013, **7**, 8366–8378.
4 Q. Zhang, I. Lee, J. B. Joo, F. Zaera and Y. Yin, *Acc. Chem. Res.*, 2013, **46**, 1816–1824.
5 C. Gao, F. Lyu and Y. Yin, *Chem. Rev.*, 2021, **121**, 834–881.
6 P. Ranadive, Z. Blanchette, A. P. Spanos, J. W. Medlin and N. A. Brunelli, *J. Flow Chem.*, 2021, 1–14.
7 K. F. Jensen, *AIChE J.*, 2017, **63**, 858–869.
8 X. Liu and X. Liu, *Angew. Chem., Int. Ed.*, 2012, **51**, 3311–3313.
9 A. Dobhal, A. Kulkarni, P. Dandekar and R. Jain, *J. Mater. Chem. B*, 2017, **5**, 3404–3417.
10 L. Wang, L. R. Karadaghi, R. L. Brutchey and N. Malmstadt, *Chem. Commun.*, 2020, **56**, 3745–3748.
11 R. L. Hartman, J. P. McMullen and K. F. Jensen, *Angew. Chem., Int. Ed.*, 2011, **50**, 7502–7519.
12 M. Jiang, Y. E. D. Li, H. H. Tung and R. D. Braatz, *Chem. Eng. Process.: Process Intesif.*, 2015, **97**, 242–247.
13 J. Zhang, K. Wang, A. R. Teixeira, K. F. Jensen and G. Luo, *Annu. Rev. Chem. Biomol. Eng.*, 2017, **8**, 285–305.
14 S. Marre and K. F. Jensen, *Chem. Soc. Rev.*, 2010, **39**, 1183–1202.
15 P. Kunal, E. J. Roberts, C. T. Riche, K. Jarvis, N. Malmstadt, R. L. Brutchey and S. M. Humphrey, *Chem. Mater.*, 2017, **29**, 4341–4350.

16 A. M. Robinson, J. E. Hensley and J. Will Medlin, *ACS Catal.*, 2016, **6**, 5026–5043.
17 M. B. Gawande, A. Goswami, T. Asefa, H. Guo, A. V. Biradar, D.-L. Peng, R. Zboril and R. S. Varma, *Chem. Soc. Rev.*, 2015, **44**, 7540–7590.
18 P. K. Kalambate, Dhanjai, Z. Huang, Y. Li, Y. Shen, M. Xie, Y. Huang and A. K. Srivastava, *TrAC, Trends Anal. Chem.*, 2019, **115**, 147–161.
19 J. Zeng, C. Zhu, J. Tao, M. Jin, H. Zhang, Z. Y. Li, Y. Zhu and Y. Xia, *Angew. Chem., Int. Ed.*, 2012, **51**, 2354–2358.
20 Y. Shin, Y. Lim, T. Kwak, J. H. Hwang, A. Georgescu, D. Huh, D. Kim and T. Kang, *Adv. Funct. Mater.*, 2020, **2007856**, 1–10.
21 A. Knauer, A. Eisenhardt, S. Krischok and J. M. Koehler, *Nanoscale*, 2014, **6**, 5230–5238.
22 L. P. Bressan, T. M. Lima, G. D. da Silveira and J. A. F. da Silva, *SN Appl. Sci.*, 2020, **2**, 1–8.
23 A. Vikram, V. Kumar, U. Ramesh, K. Balakrishnan, N. Oh, K. Deshpande, T. Ewers, P. Trefonas, M. Shim and P. J. A. Kenis, *ChemNanoMat*, 2018, **4**, 943–953.
24 D. Yang, K. Kang, D. Kim, Z. Li and I. Park, *Sci. Rep.*, 2015, **5**, 1–10.
25 O. Yang, M. Qadan and M. Ierapetritou, *J. Pharm. Innov.*, 2020, **15**, 182–200.
26 N. T. K. Thanh, N. Maclean and S. Mahiddine, *Chem. Rev.*, 2014, **114**, 7610–7630.
27 R. A. French, A. R. Jacobson, B. Kim, S. L. Isley and R. L. E. E. Penn, *Environ. Sci. Technol.*, 2009, **43**, 1354–1359.
28 J. A. Liddle and G. M. Gallatin, *ACS Nano*, 2016, **10**, 2995–3014.
29 A. Parulkar and N. A. Brunelli, *Ind. Eng. Chem. Res.*, 2017, **56**, 10384–10392.
30 P. Ranadive, A. Parulkar and N. A. Brunelli, *React. Chem. Eng.*, 2019, **4**, 1779–1789.
31 J. M. Lim, A. Swami, L. M. Gilson, S. Chopra, S. Choi, J. Wu, R. Langer, R. Karnik and O. C. Farokhzad, *ACS Nano*, 2014, **8**, 6056–6065.
32 H. Shen, S. Hong, R. K. Prud'Homme and Y. Liu, *J. Nanopart. Res.*, 2011, **13**, 4109–4120.
33 Y. Liu, Z. Tong and R. K. Prud'homme, *Pest Manage. Sci.*, 2008, **64**, 808–812.
34 V. Sebastián and K. F. Jensen, *Nanoscale*, 2016, **8**, 15288–15295.
35 Y. J. Hwang, C. W. Coley, M. Abolhasani, A. L. Marzinzik, G. Koch, C. Spanka, H. Lehmann and K. F. Jensen, *Chem. Commun.*, 2017, **53**, 6649–6652.
36 A. Günther, S. A. Khan, M. Thalmann, F. Trachsel and K. F. Jensen, *Lab Chip*, 2004, **4**, 278–286.
37 R. O. Fox, J. C. Hill and M. G. Olsen, *J. Fluids Eng.*, 2015, **137**, 2–7.
38 B. K. Johnson and R. K. Prud'homme, *Aust. J. Chem.*, 2003, 1021–1024.
39 B. K. Johnson and R. K. Prud'homme, *AIChE J.*, 2003, **49**, 2264–2282.
40 H. Mehenni, L. Sinatra, R. Mahfouz, K. Katsiev and O. M. Bakr, *RSC Adv.*, 2013, **3**, 22397.
41 D. M. Holunga, R. C. Flagan and H. A. Atwater, *Ind. Eng. Chem. Res.*, 2005, **44**, 6332–6341.
42 E. Petryayeva and U. J. Krull, *Anal. Chim. Acta*, 2011, **706**, 8–24.
43 Y. Shin, Y. Lim, T. Kwak, J. H. Hwang, A. Georgescu, D. Huh, D. Kim and T. Kang, *Adv. Funct. Mater.*, 2020, **2007856**, 1–10.
44 P. Ranadive, A. Parulkar and N. A. Brunelli, *React. Chem. Eng.*, 2019, **4**, 1779–1789.
45 C. Deraedt, L. Salmon, S. Gatard, R. Ciganda, R. Hernandez, J. Ruiz and D. Astruc, *Chem. Commun.*, 2014, **50**, 14194–14196.
46 C. A. Schneider, W. S. Rasband and K. W. Eliceiri, *Nat. Methods*, 2012, **9**, 671–675.
47 G. M. Nabar, Encapsulation of Nanoparticles and Polymers within Block Copolymer Micelles Prepared by the Emulsion and Solvent Evaporation Method, *Dissertation*, Chemical and Biomolecular Engineering, The Ohio State University, 2017.
48 K. H. Lee, F. N. Khan, L. Cosby, G. Yang and J. O. Winter, *Front. Nanotechnol.*, 2021, **3**, 1–14.
49 P. K. Jain, K. S. Lee, I. H. El-Sayed and M. A. El-Sayed, *J. Phys. Chem. B*, 2006, **110**, 7238–7248.
50 D. B. Williams and C. B. Carter, *Transmission Electron Microscopy*, 2009.
51 I. R. Baxendale, R. D. Braatz, A. J. Florence, B. K. Hodnett, K. F. Jensen, M. D. Johnson, P. Sharratt and J.-P. Sherlock, *J. Pharm. Sci.*, 2015, **104**, 781–791.
52 L. Xu, J. Peng, C. Srinivasakannan, L. Zhang, D. Zhang, C. Liu, S. Wang and A. Q. Shen, *RSC Adv.*, 2014, **4**, 25155–25159.
53 R. Baber, L. Mazzei, N. T. K. Thanh and A. Gavriilidis, *RSC Adv.*, 2015, **5**, 95585–95591.
54 A. Nour, N. Hassan, H. M. Refaat, H. M. A. Soliman and A. El-Dissouky, *Mater. Res. Express*, 2018, **5**, 35033.
55 S. Agnihotri, S. Mukherji and S. Mukherji, *RSC Adv.*, 2014, **4**, 3974–3983.
56 B. Michen, C. Geers, D. Vanhecke, C. Endes, B. Rothen-Rutishauser, S. Balog and A. Petri-Fink, *Sci. Rep.*, 2015, **5**(1), 9793.
57 J. A. Mascorro, *Microsc. Today*, 2003, 47–48.
58 E. Bolea, J. Jiménez-Lamana, F. Laborda and J. R. Castillo, *Anal. Bioanal. Chem.*, 2011, **401**, 2723–2732.
59 T. J. Cho and V. A. Hackley, *Anal. Bioanal. Chem.*, 2010, **398**, 2003–2018.